LETTERS
https://doi.org/10.1038/s41567-020-0839-3

nature physics

Check for updates

Pattern formation in a driven Bose–Einstein condensate

Zhendong Zhang[1,2,3], Kai-Xuan Yao[1,2,3], Lei Feng[1,2,3], Jiazhong Hu[4,5,6] and Cheng Chin[1,2,3] ✉

Pattern formation is ubiquitous in nature at all scales, from morphogenesis and cloud formation to galaxy filamentation. How patterns emerge in a homogeneous system is a fundamental question across interdisciplinary research including hydrodynamics[1], condensed matter physics[2], nonlinear optics[3], cosmology[4] and bio-chemistry[5,6]. Paradigmatic examples, such as Rayleigh–Bénard convection rolls and Faraday waves[7,8], have been studied extensively and found numerous applications[9–11]. How such knowledge applies to quantum systems and whether the patterns in a quantum system can be controlled remain intriguing questions. Here we show that the density patterns with two- (D_2), four- (D_4) and six-fold (D_6) symmetries can emerge in Bose–Einstein condensates on demand when the atomic interactions are modulated at multiple frequencies. The D_6 pattern, in particular, arises from a resonant wave-mixing process that establishes phase coherence of the excitations that respect the symmetry. Our experiments explore a novel class of non-equilibrium phenomena in quantum gases, as well as a new route to prepare quantum states with desired correlations.

In classical systems, the onset of pattern formation can be understood from the dynamics and interaction of the excitations in momentum space, described by the nonlinear amplitude equation[12–15]

$$\frac{\mathrm{d}u_i}{\mathrm{d}t} = \alpha_i u_i + \sum_{j,k} \beta_{ijk} u_j u_k + O(u^3) \tag{1}$$

where u_i is the amplitude of the ith excitation mode. Starting from small amplitudes, the modes grow exponentially at rate α_i. The quadratic term becomes important as the mode grows, and the tensor β_{ijk} describes the mixing of the modes and determines the resulting pattern. The explicit form of β_{ijk} is given by the underlying physics, for example, by the Navier–Stokes equation for hydrodynamic systems[16,17].

In quantum systems, patterns—often characterized by correlation functions—frequently arise from long-range interactions or dynamics far from equilibrium. In polaritonic quantum fluids, hexagonal patterns emerge due to scattering between polaritons[18]. In cold atoms, Faraday waves induced by the modulation of trap frequency[19,20] or interactions[21,22] occur in one-dimensional (1D) Bose–Einstein condensates (BECs). BECs also develop spin[23] or density wave patterns[24] by quenching of atomic interactions. Droplets in a dipolar BEC form a hexagonal pattern due to Rosensweig instability[25]. Recently, supersolid order, for which a superfluid exhibits spatial correlations, emerges in condensates with spin–orbit coupling[26] or dipolar interactions[27–29].

In this Letter, we report the formation of various 2D density wave patterns in a uniform BEC by modulating the atomic interactions at two frequencies in the vicinity of a Feshbach resonance (Fig. 1a). The interaction modulation is realized by applying an oscillating magnetic field to the sample[30,31]. The magnetic field is in the z direction perpendicular to the sample, while the pattern forms in the horizontal $x-y$ plane (Fig. 1b). By changing the ratio of the two modulation frequencies, density patterns with D_2, D_4 and D_6 symmetries were observed in situ and analysed. The D_6 density wave pattern, in particular, results from a novel coherent process that resonantly couples six momentum modes.

To understand the pattern formation process in a driven condensate, we derive the associated quantum nonlinear amplitude equation as (see Methods)

$$\frac{\mathrm{d}\hat{a}_{\mathbf{k}}}{\mathrm{d}t} = \gamma_1 \hat{a}^\dagger_{-\mathbf{k}} + \gamma_2 \sum_{\mathbf{k}_1} \hat{a}^\dagger_{\mathbf{k}_1-\mathbf{k}} \hat{a}_{\mathbf{k}_1} - \gamma_2^* \sum_{\mathbf{k}_2} \hat{a}_{\mathbf{k}_2} \hat{a}_{\mathbf{k}-\mathbf{k}_2} \tag{2}$$

where $\hat{a}_{\mathbf{k}}$ and $\hat{a}^\dagger_{\mathbf{k}}$ are the bosonic annihilation and creation operators with momentum $\hbar\mathbf{k}$, respectively, $\hbar = h/2\pi$ is the reduced Planck constant, the summations include all resonant scattering processes, and the rate constants γ_1 and γ_2 are given by the modulation strengths. This equation is reminiscent of the classical amplitude equation (1).

The wave-mixing processes leading to D_4 and D_6 patterns can be described in two stages (Fig. 1c). In the seeding stage, atom pairs with opposite momentum are generated from the condensate by a single-frequency modulation. Such a process, given by the first term in equation (2), seeds and amplifies the primary excitations that spontaneously break the rotational symmetry of the system. In the pattern-forming stage, the same or a different frequency component is introduced to the modulation, which stimulates scatterings into a particular pattern with the desired symmetry (see Methods). This process is described by the nonlinear terms in equation (2). Finally, the excitation modes interfere with the BEC to form the density wave $n(\mathbf{r})$, which we observe. The density wave relates to the excitations $\hat{a}_{\mathbf{k}}$ as $\hat{n}(\mathbf{r}) = n_0(\hat{1} + N_0^{-1/2}\sum_{\mathbf{k}}(\hat{a}_{\mathbf{k}} + \hat{a}^\dagger_{-\mathbf{k}})e^{i\mathbf{k}\cdot\mathbf{r}})$, where n_0 is the condensate density and $N_0 \gg 1$ is the atom number in the condensate. We emphasize that the spatial symmetry of the patterns is only controlled by the ratio of the modulation frequencies, and the sample is collisionally thin. These are in contrast to previous Faraday wave experiments[9,10,19–22], where the patterns rely on the strength of the modulation amplitudes and relaxation in the hydrodynamic regime.

[1]James Franck Institute, University of Chicago, Chicago, IL, USA. [2]Enrico Fermi Institute, University of Chicago, Chicago, IL, USA. [3]Department of Physics, University of Chicago, Chicago, IL, USA. [4]Department of Physics, Tsinghua University, Beijing, China. [5]State Key Laboratory, Tsinghua University, Beijing, China. [6]Frontier Science Center for Quantum Information, Beijing, China. ✉e-mail: cchin@uchicago.edu

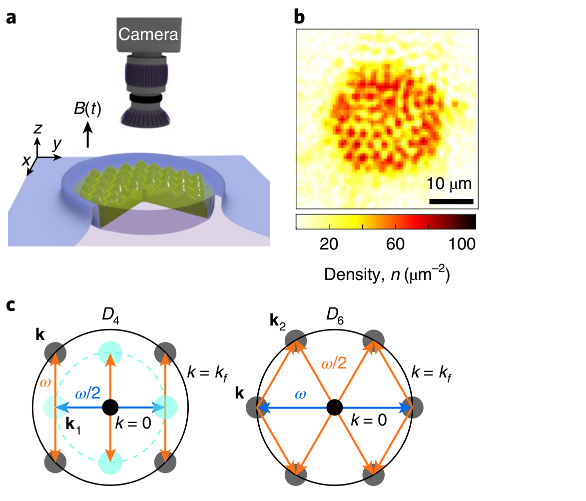

Fig. 1 | Pattern formation in a BEC with interaction modulation at two frequencies. a, A BEC (green) of ^{133}Cs atoms is trapped in a 2D circular potential well (blue). An oscillating magnetic field $B(t)$ in the z direction modulates the scattering length. The atomic density is recorded by a camera. **b**, An example image of the driven BEC showing density waves. **c**, Scattering processes that generate D_4 and D_6 density waves are illustrated in momentum space in two stages. In the seeding stage, the BEC (black dot) at wavenumber $k=0$ produces atom pairs with opposite momentum (blue arrows). In the pattern-forming stage, collisions between the atom pairs and the BEC generate four or six modes with wavenumber $|\mathbf{k}|=k_f$ (orange arrows; see main text) with equal angular spacing, which we study in this work. For the creation of D_4 and D_6 patterns, the modulation frequencies are $\omega/2$ followed by ω, and ω followed by $\omega/2$, respectively. Cyan circles indicate other modes populated during the scattering processes.

The experiment starts with a BEC of $N_0 = 60{,}000$ Cs atoms in a 2D dipole trap. Atoms are radially confined in a uniform circular potential well with a radius of 14.5 μm and a barrier height of $h \times 140$ Hz. In the vertical direction, the sample is confined in a harmonic potential with a $1/e^2$ radius of 0.78 μm. We then apply an oscillating magnetic field near a Feshbach resonance[32] to the BEC, which modulates the atomic s-wave scattering length a. After modulation time t, we perform in situ imaging to record the density waves (see Methods).

We first describe the experimental procedure for the formation of the density waves with D_6 symmetry. In the seeding stage, we apply a single-frequency modulation as $a(t) = a_{\rm dc} + a_1 \sin \omega t$, where $\omega/2\pi = 450$ Hz, $a_1 = 30a_0$, $a_{\rm dc} = 2a_0$ and a_0 is the Bohr radius. After $t = 22.2$ ms, in the pattern-forming stage, we add a second frequency component to the modulation as $a(t) = a_{\rm dc} + a_1 \sin \omega t + a_2 \sin \omega t/2$, where $a_2 = 25a_0$ (Fig. 2a).

We analyse the symmetry of the density wave patterns based on Fourier analysis. In the seeding stage, only stripe patterns appear. In the pattern-forming stage, hexagonal lattice patterns with D_6 symmetry emerge, signified by six distinct modes in the Fourier space. The modes are equally spaced by $\pi/3$ in directions with the same wavenumber $k_f = \sqrt{m\omega/\hbar} = 2.43\ \mu\text{m}^{-1}$ (ref. [30] and Fig. 2b), where m is the atomic mass.

The presence of the D_6 pattern can be further confirmed with a pattern recognition algorithm[33] (Fig. 2c). To quantify the strength of the patterns, we evaluate the density correlation function $g^{(2)}(\theta) \equiv \langle |A_\varphi|^2 |A_{\varphi+\theta}|^2 \rangle / \langle |A_\varphi|^2 \rangle^2$, where $A_\theta = \int n(\mathbf{r}) e^{-i\mathbf{k}_\theta \cdot \mathbf{r}} d\mathbf{r}$ is the Fourier amplitude evaluated at $\mathbf{k}_\theta$ with magnitude $|\mathbf{k}_\theta| = k_f$ and angle θ. The angle brackets denote averaging over both the angle φ from 0 to 2π and the images. The evolution of $g^{(2)}$ confirms the growth of different patterns in the seeding and pattern-forming stages (Fig. 2c).

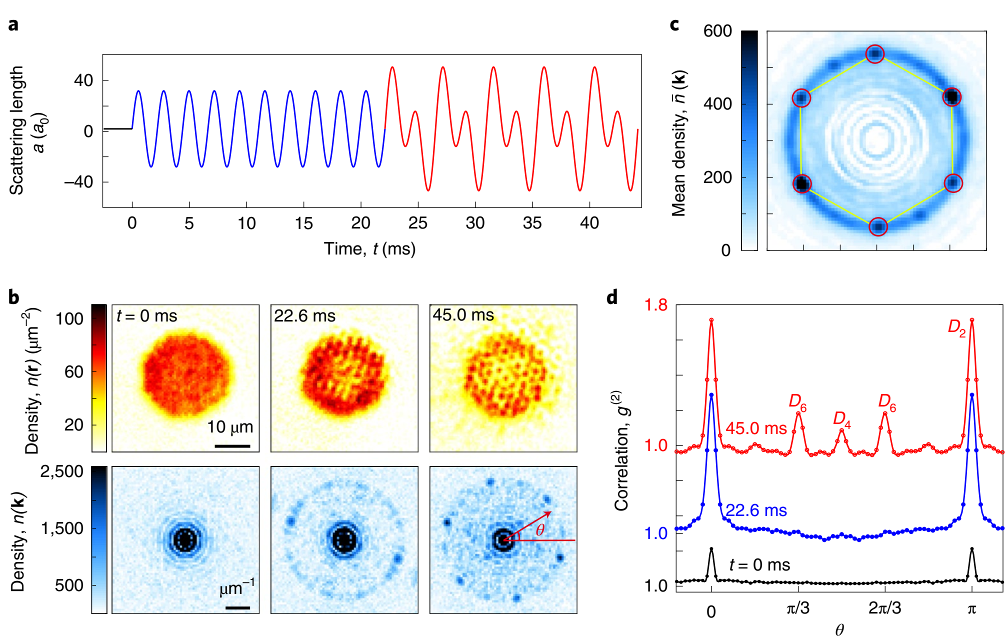

Fig. 2 | Formation of density waves with D_6 symmetry. a, The scattering length is modulated in two stages. The modulation frequency is 450 Hz in the first 10 cycles; this is then superposed with a second modulation of 225 Hz (see main text). **b**, Examples of in situ images at $t = 0$, 22.6 and 45.0 ms (top row) and the corresponding Fourier transforms (bottom row). At 45 ms, the Fourier transform displays six peaks with $\pi/3$ angular spacing that break rotation symmetry. The six-peak patterns orient randomly in repeated experiments. **c**, Pattern recognition based on 185 Fourier-transformed images yields six strong peaks (red circles) on the vertices of a hexagon (yellow). Two weaker peaks arise from patterns with D_4 symmetry. We remove the contribution from the BECs (see Methods). **d**, Correlations $g^{(2)}$ of the Fourier modes with angular spacing θ. The peaks at $\pi/3$, $\pi/2$ and π indicate the strength of the patterns with D_6, D_4 and D_2 symmetry, respectively.

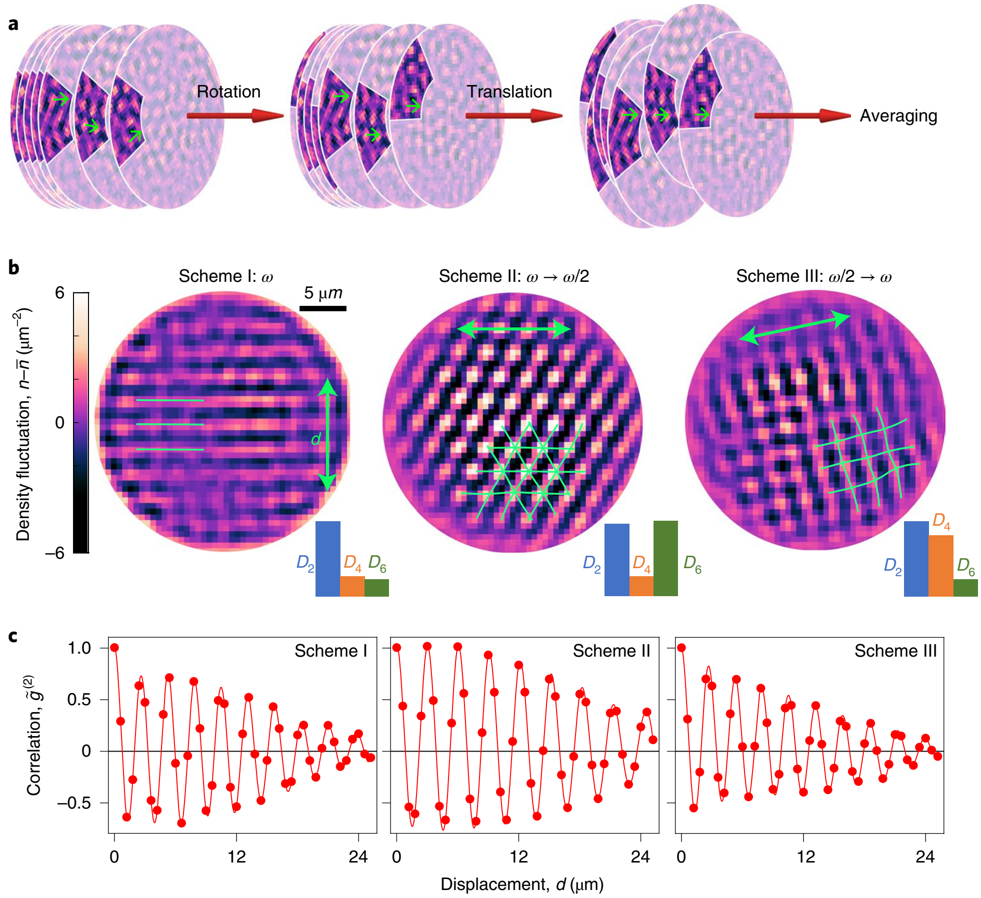

Fig. 3 | Density wave patterns in real space. a, In our pattern recognition algorithm, each of the in situ images is first rotated and then translated to overlap the density waves. The translation maximizes the variance of the averaged image (see Methods). **b**, Resulting density waves from the algorithm: scheme I (stripes), with single modulation frequency ω; scheme II (hexagonal lattice), with ω followed by $\omega/2$; scheme III (square lattice), with $\omega/2$ followed by ω. The green lines are guides to the eye to highlight the corresponding pattern. The green arrows show the direction along which the real-space correlation is evaluated in **c**. The bar diagrams show the relative weights of D_2, D_4 and D_6 symmetry components from fitting the patterns (see Methods). **c**, Real-space correlation functions evaluated from the patterns. The oscillations have periods of 2.63(1), 3.05(1) and 2.65(1) μm for schemes I, II and III, respectively. The ratio of the periods is 1.156(2), consistent with the theory value of $2/\sqrt{3}\approx 1.155$. The solid lines are guides to the eye.

We tailor the modulation waveform to create different patterns. Here, three modulation schemes that lead to patterns with D_2, D_4 and D_6 symmetries are reported. In scheme I, we apply the modulation at a single frequency ω. In scheme II, we modulate at frequency ω in the seeding stage and superpose a second frequency $\omega/2$ in the pattern-forming stage (Fig. 2a). In scheme III, we modulate at frequency $\omega/2$ and then switch to frequency ω.

To reveal the density patterns in real space, we use a 2D pattern recognition algorithm. Because the pattern in each image appears with random orientation and displacement, the algorithm is developed to rotate and align the patterns (Fig. 3a). We determine the orientation of each image as illustrated in Fig. 2c, and align all of them in the same direction. We then translate each of the images independently to maximize the spatial variance of their average. Finally, we extract the underlying pattern by averaging all aligned images. To eliminate long wavelength variations that are uncorrelated with the pattern and to only focus on patterns formed at the wavelength corresponding to k_f, we filter the density fluctuations at $|\mathbf{k}|\leq 0.75k_f$ from the images to obtain the density waves $\tilde{n}(\mathbf{r})$.

The results of the 2D pattern recognition algorithm are shown in Fig. 3b. Single-frequency modulation (scheme I) produces D_2 stripe patterns. Scheme II ($\omega\rightarrow\omega/2$) results in a hexagonal lattice pattern, consistent with Fig. 2. Scheme III ($\omega/2\rightarrow\omega$) results in a square lattice pattern. We further determine the strengths of different symmetry components in each image P based on the fit $P=c_2P_2+c_4P_4+c_6P_6$, where P_n are normalized patterns with D_n symmetry and c_n are the fitting parameters (see Methods). The results, shown in the bar diagrams of Fig. 3b, suggest that different schemes are effective in generating patterns with different symmetries.

Remarkably, all three patterns extend throughout the entire sample. The spatial extent of the patterns can be evaluated from their real-space correlation functions $\tilde{g}^{(2)}(\mathbf{r})\equiv\int\tilde{n}(\mathbf{r}_0)\tilde{n}(\mathbf{r}_0+\mathbf{r})\mathrm{d}\mathbf{r}_0/\int\tilde{n}^2(\mathbf{r}_0)\mathrm{d}\mathbf{r}_0$. Correlations along principle directions, shown in Fig. 3c, extend across the entire sample of diameter 25 μm. We note that the finite correlations of the 2D superfluid might limit the correlation length we report here. Comparing the patterns, we observe that the D_6 pattern is a factor of 5 more pronounced than D_4, even though these two schemes employ similar modulation strengths (see Methods).

The clear difference between the strengths of the D_4 and D_6 patterns comes from the coherence of the underlying scattering processes. For D_4 patterns, phase coherence only exists between counter-propagating modes. The orthogonal modes are generated from independent scattering processes and are phase-independent, as illustrated in Fig. 4a. We evaluate the two-point phase correlation function of the density waves as $g^{(1)}(\theta)\equiv\langle A_\varphi A_{\varphi+\theta}\rangle/\langle|A_\varphi|^2\rangle$, where $A_\theta=|A_\theta|\mathrm{e}^{i\phi_\theta}$ is the Fourier amplitude of the mode with wavenumber k_f at angle θ and ϕ_θ is its phase. The result (Fig. 4b) shows a single

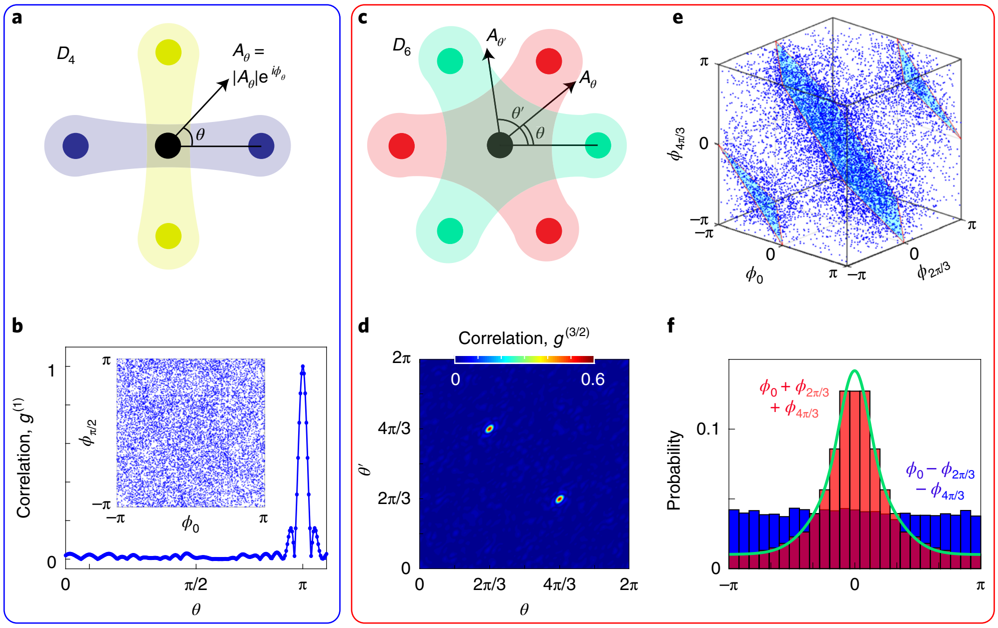

Fig. 4 | Coherent properties of D_4 and D_6 density waves. a, Pairs of modes with opposite momenta (blue and yellow) are phase-correlated in the D_4 density wave pattern. **b**, The phase correlation function $g^{(1)}$ between Fourier components of the density wave is evaluated based on 123 images obtained with scheme III. Strong correlations appear between modes moving in opposite directions $\theta=\pi$, but not perpendicular modes $\theta=\pi/2$. Inset: histogram of the phase of perpendicular modes $\pi/2$, which shows no discernable correlation. **c**, Three-point phase coherence appears in triplet modes (green and red) of the D_6 density wave pattern. **d**, The phase correlation function $g^{(3/2)}$ of three Fourier amplitudes separated by angles θ and θ', evaluated based on 185 images with scheme III, shows two peaks at $(\theta,\theta')=(2\pi/3, 4\pi/3)$ and $(4\pi/3, 2\pi/3)$, supporting phase correlations of the triplets. **e**, Phases of three modes separated by $2\pi/3$ and $4\pi/3$ show higher probability near the planes $\phi_0+\phi_{2\pi/3}+\phi_{4\pi/3}=0, \pm2\pi$ (blue planes). **f**, The probability distribution (red) of the phase $\phi_0+\phi_{2\pi/3}+\phi_{4\pi/3}$ weighted by the atom number of the triplet modes displays a peak at 0 (red bars). An alternative combination of the phases, $\phi_0-\phi_{2\pi/3}-\phi_{4\pi/3}$, is evenly distributed (blue bars). The green curve is from the numerical calculation (see Supplementary Information).

peak at $\theta=\pi$, simply due to the realness of density. The absence of other features, particularly at $\theta=\pi/2$, shows that the density waves in orthogonal directions are incoherent. Close inspection of the phases of orthogonal modes (inset, Fig. 4b) confirms the absence of correlation.

The D_6 pattern, on the other hand, displays a novel phase coherence in triplets of modes angularly spaced by $2\pi/3$ (Fig. 4c). Here we evaluate the three-point phase correlation function as

$$g^{(3/2)}(\theta,\theta') \equiv \frac{\langle A_\varphi A_{\varphi+\theta} A_{\varphi+\theta'}\rangle}{\sqrt{\langle |A_\varphi|^2\rangle\langle |A_{\varphi+\theta}|^2\rangle\langle |A_{\varphi+\theta'}|^2\rangle}} \quad (3)$$

The correlation shows two peaks at $(\theta,\theta')=(2\pi/3,4\pi/3)$ and $(4\pi/3, 2\pi/3)$ (Fig. 4d), where θ and θ' are the relative angles between the three modes. This indicates phase coherence of any three modes angularly separated by $2\pi/3$. From repeated measurements, we find that the phases of the triplets are statistically constrained to $\phi_0+\phi_{2\pi/3}+\phi_{4\pi/3}=0$ modulo 2π with a small standard deviation of $\delta\phi=1.1$ (Fig. 4e,f). The phase differences, for example $\phi_0-\phi_{2\pi/3}-\phi_{4\pi/3}$, as well as other permutations, are uniformly distributed and thus uncorrelated.

The three-point phase correlation is an essential element to understanding the growth and origin of D_6 patterns in our system. Based on equation (2), we show that the strength of the D_6 pattern satisfies the equation of motion (see Supplementary Information)

$$\frac{dA_{\rm rms}}{dt} = \gamma_1 A_{\rm rms} + \gamma_2 g^{(3/2)} A^2_{\rm rms} \quad (4)$$

where $A_{\rm rms}$ is the root-mean square of the six Fourier amplitudes that constitute the D_6 pattern and $g^{(3/2)} \equiv g^{(3/2)}(2\pi/3, 4\pi/3)$. A positive $g^{(3/2)}$ suggests that, beyond small amplitudes, the nonlinear wave-mixing term dominates and leads to a faster-than-exponential (hyperbolic) growth of the D_6 density waves. The large measured value of $g^{(3/2)}=0.58$ explains the strong D_6 pattern that we observe.

How does the three-point phase correlation emerge in a driven condensate? Starting from a condensate seeded by the single-frequency modulation, we see that $g^{(3/2)}$ increases quickly from zero after the two-frequency modulation starts (see Supplementary Information). Theoretically, the growth of the correlation is linked to the resonant nonlinear coupling of excitation modes that respect the symmetry and is described by $dg^{(3/2)}/dt = 3\gamma_2 A_{\rm rms}$ for small amplitudes $A_{\rm rms} << N_0^{1/2}$. Our measurement is in good agreement with the theory (see Supplementary Information). Given the above, the three-point phase relation $\phi_0+\phi_{2\pi/3}+\phi_{4\pi/3}=0$ (Fig. 4f) can be understood as the phase-matching condition that maximizes the correlator $g^{(3/2)}$, which explains the dominance of the D_6 pattern in our experiment.

Our experiments thus provide insights into the origin of pattern formation from the coherent mixing of excitations in a homogeneous system. The pattern formation represents a new form of quantum dynamics in which spatial symmetries are determined by the temporal modulation. Moreover, the excitation modes associated with the patterns are phase-correlated in a unique way and the modes are expected to be entangled (see Methods). These patterns can thus serve as a resource of multimode entanglement for applications in quantum control and quantum information processing.

Online content

Any methods, additional references, Nature Research reporting summaries, source data, extended data, supplementary information, acknowledgements, peer review information; details of author contributions and competing interests; and statements of data and code availability are available at https://doi.org/10.1038/s41567-020-0839-3.

Received: 11 October 2019; Accepted: 12 February 2020;
Published online: 23 March 2020

References

1. Cross, M. C. & Hohenberg, P. C. Pattern formation outside of equilibrium. *Rev. Mod. Phys.* **65**, 851–1112 (1993).
2. Mouritsen, O. G. Pattern formation in condensed matter. *Int. J. Modern Phys. B* **04**, 1925–1954 (1990).
3. Arecchi, F., Boccaletti, S. & Ramazza, P. Pattern formation and competition in nonlinear optics. *Phys. Rep.* **318**, 1–83 (1999).
4. Liddle, A. R. & Lyth, D. H. *Cosmological Inflation and Large-Scale Structure* (Cambridge Univ. Press, 2000).
5. Turing, A. M. The chemical basis of morphogenesis. *Phil. Trans. R. Soc. Lond. B Biol. Sci.* **237**, 37–72 (1952).
6. Maini, P. K., Painter, K. J. & Chau, H. N. P. Spatial pattern formation in chemical and biological systems. *J. Chem. Soc. Faraday Trans.* **93**, 3601–3610 (1997).
7. Bodenschatz, E., Pesch, W. & Ahlers, G. Recent developments in Rayleigh–Bénard convection. *Annu. Rev. Fluid Mech.* **32**, 709–778 (2000).
8. Miles, J. On Faraday waves. *J. Fluid Mech.* **248**, 671–683 (1993).
9. Edwards, W. S. & Fauve, S. Patterns and quasi-patterns in the Faraday experiment. *J. Fluid Mech.* **278**, 123–148 (1994).
10. Lifshitz, R. & Petrich, D. M. Theoretical model for Faraday waves with multiple-frequency forcing. *Phys. Rev. Lett.* **79**, 1261–1264 (1997).
11. Arbell, H. & Fineberg, J. Pattern formation in two-frequency forced parametric waves. *Phys. Rev. E* **65**, 036224 (2002).
12. Swift, J. & Hohenberg, P. C. Hydrodynamic fluctuations at the convective instability. *Phys. Rev. A* **15**, 319–328 (1977).
13. Pomeau, Y. & Manneville, P. Intermittent transition to turbulence in dissipative dynamical systems. *Commun. Math. Phys.* **74**, 189–197 (1980).
14. Sakaguchi, H. & Brand, H. R. Localized patterns for the quintic complex Swift–Hohenberg equation. *Physica D* **117**, 95–105 (1998).
15. Hoyle, R. *Pattern Formation: An Introduction to Methods* (Cambridge Univ. Press, 2006).
16. Landau, L. D. & Lifshitz, E. M. *Fluid Mechanics* Vol. 6 (Course of Theoretical Physics, Pergamon Press, 1959).
17. Temam, R. & Chorin, A. *Navier Stokes Equations: Theory and Numerical Analysis* (AMS Chelsea Publishing, 1978).
18. Ardizzone, V. et al. Formation and control of Turing patterns in a coherent quantum fluid. *Sci. Rep.* **3**, 3016 (2013).
19. Engels, P., Atherton, C. & Hoefer, M. A. Observation of Faraday waves in a Bose–Einstein condensate. *Phys. Rev. Lett.* **98**, 095301 (2007).
20. Groot, A. *Excitations in Hydrodynamic Ultra-Cold Bose Gases*. PhD thesis, Utrecht Univ. (2015).
21. Nguyen, J. H. V. et al. Parametric excitation of a Bose–Einstein condensate: from Faraday waves to granulation. *Phys. Rev. X* **9**, 011052 (2019).
22. Pollack, S. E. et al. Collective excitation of a Bose–Einstein condensate by modulation of the atomic scattering length. *Phys. Rev. A* **81**, 053627 (2010).
23. Kronjäger, J., Becker, C., Soltan-Panahi, P., Bongs, K. & Sengstock, K. Spontaneous pattern formation in an antiferromagnetic quantum gas. *Phys. Rev. Lett.* **105**, 090402 (2010).
24. Hung, C.-L., Gurarie, V. & Chin, C. From cosmology to cold atoms: observation of Sakharov oscillations in a quenched atomic superfluid. *Science* **341**, 1213–1215 (2013).
25. Kadau, H. et al. Observing the Rosensweig instability of a quantum ferrofluid. *Nature* **530**, 194–197 (2016).
26. Li, J.-R. et al. A stripe phase with supersolid properties in spin–orbit-coupled Bose–Einstein condensates. *Nature* **543**, 91–94 (2017).
27. Böttcher, F. et al. Transient supersolid properties in an array of dipolar quantum droplets. *Phys. Rev. X* **9**, 011051 (2019).
28. Tanzi, L. et al. Observation of a dipolar quantum gas with metastable supersolid properties. *Phys. Rev. Lett.* **122**, 130405 (2019).
29. Chomaz, L. et al. Long-lived and transient supersolid behaviors in dipolar quantum gases. *Phys. Rev. X* **9**, 021012 (2019).
30. Clark, L. W., Gaj, A., Feng, L. & Chin, C. Collective emission of matter-wave jets from driven Bose–Einstein condensates. *Nature* **551**, 356–359 (2017).
31. Fu, H. et al. Density waves and jet emission asymmetry in Bose fireworks. *Phys. Rev. Lett.* **121**, 243001 (2018).
32. Chin, C., Grimm, R., Julienne, P. & Tiesinga, E. Feshbach resonances in ultracold gases. *Rev. Mod. Phys.* **82**, 1225–1286 (2010).
33. Feng, L., Hu, J., Clark, L. W. & Chin, C. Correlations in high-harmonic generation of matter-wave jets revealed by pattern recognition. *Science* **363**, 521–524 (2019).

Methods

Experimental procedure. We started with BECs of 60,000 Cs atoms loaded into a disk-shaped dipole trap with a radius of 14.5 μm in the horizontal direction. The horizontal confinement was provided by a blue-detuned laser at 780 nm. We shaped the laser beam profile using a digital micromirror device and projected it to the atom plane through a high-resolution objective. The resulting circular potential well has a barrier height of $h \times 140$ Hz. The uniformity of the potential well is reflected by the atomic density profile at the beginning of the modulation, as shown in Fig. 2b, where the variation is ~10% of the mean density. Atoms are tightly confined in the vertical direction with a $1/e^2$ radius of 0.78 μm and a harmonic trap frequency of 259 Hz.

After preparing the sample, we modulated the magnetic field near a Feshbach resonance, which caused the *s*-wave scattering length a of the atoms to oscillate as $a(t) = a_{dc} + a_1(t)\sin\omega_1 t + a_2(t)\sin(\omega_2 t + \phi)$. We used an arbitrary waveform generator to control the current modulation in the coils, leading to the magnetic field being modulated according to a designed waveform. A small positive offset scattering length $a_{dc} = 2a_0$ was maintained throughout the experiment to keep the condensate stable. Because the chemical potential was much smaller than the vertical trapping frequency, the BEC was in the quasi-2D regime[37]. To generate the D_2 density wave pattern, we modulated the scattering length at frequency 450 Hz with amplitude $45a_0$ for 23.8 ms. For the D_4 pattern, we first modulated at 225 Hz for three cycles with amplitude $45a_0$ and then switched to 450 Hz with the same amplitude for 24 ms. To generate the D_6 pattern, the first 10 cycles of modulation were at 450 Hz with amplitude $30a_0$; this was then mixed with another frequency component at 225 Hz and amplitude $25a_0$ for 22.8 ms. The relative phase ϕ between these two frequency components was 0. The modulation frequencies we employed did not match the vertical trap frequency, and thus the atomic motion in the vertical direction was not excited. This distinguishes our experiment from previous Faraday wave experiments on BECs[19,22,34]. In addition, it is only important that the two modulation frequencies have the proper ratio of 1:2 or 2:1 to ensure the phase-matching condition. The specific value of any single frequency is unimportant.

We finally performed in situ absorption imaging to observe the resulting density waves in condensates using the high-resolution objective and a charge-coupled device camera. Our imaging system is sensitive to density fluctuations of spatial frequency ranging from 0 to 3.44 μm^{-1} (ref. [35]), which covers the density waves we observed at $k_f = 2.43$ μm^{-1}.

To extract the population of excited modes from their interference with the condensate, we first Fourier-transformed the images including density waves. Then, in the Fourier space, we focused on the ring at $|k - k_f| \leq 0.1k_f$ and cut it using angular slices of 3° to count the average Fourier magnitude A_θ in the direction at angle θ. In general, the sensitivity of our imaging system varied for signals with different wavenumber. We measured the modulation transfer function $M(\mathbf{k})$ of thermal atoms and found that the proportional constant of measured strength of density fluctuations at k_f to its corresponding real strength was $M(k = k_f) = 0.45$ (ref. [35]). The relation between density wave amplitude A_θ and population $|a_\mathbf{k}|^2$ is $|A_\theta|^2 = 4N_0\cos^2(\omega t/2)|a_\mathbf{k}|^2$, and the phase was equal to $\omega t/2 \approx 0.57$ rad at the time of imaging. Finally, the population was evaluated as $|a_\mathbf{k}|^2 = |A_\theta|^2/[M^2(k = k_f)4N_0\cos^2(\omega t/2)]$. Also, the density waves were observed stroboscopically every 4.4 ms.

Quantum dynamics of pattern formation. We start from the general form of the Hamiltonian of driven BECs:

$$\begin{aligned} H &= \int d^3\mathbf{r}\Psi^\dagger(\mathbf{r},t)\frac{p^2}{2m}\Psi(\mathbf{r},t) + \int d^3\mathbf{r}\Psi^\dagger(\mathbf{r},t)V(\mathbf{r})\Psi(\mathbf{r},t) \\ &+ \frac{g(t)}{2}\int d^3\mathbf{r}\Psi^\dagger(\mathbf{r},t)\Psi^\dagger(\mathbf{r},t)\Psi(\mathbf{r},t)\Psi(\mathbf{r},t) \end{aligned} \tag{5}$$

where the interaction strength is modulated as $g(t) = \frac{4\pi\hbar^2}{m}[a_{dc} + a_1(t)\sin\omega_1 t + a_2(t)\sin(\omega_2 t + \phi)]$. Here, a_{dc} is a small offset scattering length to keep the condensate stable, $a_{1,2}$ are the amplitudes of the scattering length modulation and ϕ is the relative phase between the two frequency components ω_1 and ω_2.

The external potential $V(\mathbf{r})$ is neglected later because it only serves to determine the initial wavefunction of the BECs and does not affect the dynamics. After doing the Fourier transform $\Psi(\mathbf{r}) = \frac{1}{\sqrt{V}}\sum_\mathbf{k}\hat{a}_\mathbf{k}e^{i\mathbf{k}\cdot\mathbf{r}}$, we obtain the Hamiltonian in momentum space as

$$H = \sum_\mathbf{k}\epsilon_\mathbf{k}\hat{a}^\dagger_\mathbf{k}a_\mathbf{k} + \frac{g(t)}{2V}\sum_{\mathbf{k}_1,\mathbf{k}_2,\Delta\mathbf{k}}\hat{a}^\dagger_{\mathbf{k}_1+\Delta\mathbf{k}}\hat{a}^\dagger_{\mathbf{k}_2-\Delta\mathbf{k}}\hat{a}_{\mathbf{k}_1}\hat{a}_{\mathbf{k}_2} \tag{6}$$

where V is the volume of condensate and the dispersion is $\epsilon_\mathbf{k} = \hbar^2k^2/2m$.

After transferring to the rotating frame with $\hat{a}_\mathbf{k} \to \hat{a}_\mathbf{k}e^{-i\epsilon_\mathbf{k}t/\hbar}$ and using the rotating wave approximation to eliminate the fast oscillating terms, the Hamiltonian becomes time-independent:

$$H_I = \frac{i}{4V}\Big(\sum_\mathbf{k}g_1\hat{a}^\dagger_\mathbf{k}\hat{a}^\dagger_{-\mathbf{k}}\hat{a}_0\hat{a}_0 + \sum_{\mathbf{k}'}g_2\hat{a}^\dagger_{\mathbf{k}'}\hat{a}^\dagger_{-\mathbf{k}'}\hat{a}_0\hat{a}_0 + \sum_{\mathbf{k}_1,\mathbf{k}_2}g_2e^{-i\phi}\hat{a}^\dagger_{\mathbf{k}_2}\hat{a}^\dagger_{\mathbf{k}_1-\mathbf{k}_2}\hat{a}_{\mathbf{k}_1}\hat{a}_0\Big) + \text{h.c} \tag{7}$$

where $g_1 = 4\pi\hbar^2a_1/m$ and $g_2 = 4\pi\hbar^2a_2/m$ and the summations go over the processes that satisfy the following energy conservation conditions:

$$\begin{aligned} \epsilon_\mathbf{k} + \epsilon_{-\mathbf{k}} &= \hbar\omega_1 \\ \epsilon_{\mathbf{k}'} + \epsilon_{-\mathbf{k}'} &= \hbar\omega_2 \\ \epsilon_{\mathbf{k}_2} + \epsilon_{\mathbf{k}_1-\mathbf{k}_2} &= \epsilon_{\mathbf{k}_1} + \hbar\omega_2 \end{aligned} \tag{8}$$

Here, the left- and right-hand sides are the total energy after and before the collision.

The equation of motion for $\hat{a}_\mathbf{k}$ is then obtained to second order in the Bogoliubov approximation $\hat{a}_0 \approx \hat{a}^\dagger_0 \approx \sqrt{N_0}$ as

$$\frac{d\hat{a}_\mathbf{k}}{dt} = \gamma_1\hat{a}^\dagger_{-\mathbf{k}} + \gamma_2\sum_{\mathbf{k}_1}\hat{a}^\dagger_{\mathbf{k}_1-\mathbf{k}}\hat{a}_{\mathbf{k}_1} - \gamma_2^*\sum_{\mathbf{k}_2}\hat{a}_{\mathbf{k}_2}\hat{a}_{\mathbf{k}-\mathbf{k}_2} \tag{9}$$

where the growth rates are given by $\gamma_1 = \frac{N_0\pi\hbar a_1}{mV}$ and $\gamma_2 = \frac{\sqrt{N_0}\pi\hbar a_2}{mV}e^{-i\phi}$. Here, all the momenta are restricted to the horizontal plane and the magnitude of $\mathbf{k}$ is $|\mathbf{k}| = k_f = \sqrt{m\omega_1/\hbar}$. We have been using $\omega_1 = \omega = 2\pi \times 450$ Hz and $\omega_2 = \omega/2 = 2\pi \times 225$ Hz.

The formation of density wave patterns originates from the momentum and energy conservation of the underlying bosonic stimulated scattering processes (Fig. 1c). For D_4 pattern formation under scheme III, during the first modulation of frequency $\omega/2$, a pair of BEC atoms absorb a quantum of energy $\hbar\omega/2$ and scatter into a pair of atoms with opposite momenta $\pm\mathbf{k}_1$ at $|\mathbf{k}_1| = k_f/\sqrt{2}$ and energy $\epsilon_{\mathbf{k}_1} = \hbar\omega/4$. Then, one atom with $\mathbf{k}_1$ collides with one BEC atom, absorbing another quantum of $\hbar\omega/2$. One of them scatters into $\mathbf{k}$ with magnitude k_f and energy $\epsilon_\mathbf{k} = \hbar\omega/2$ at 45° (or −45°) relative to $\mathbf{k}_1$. The other is scattered into $\mathbf{k}_1 - \mathbf{k}$ with magnitude $k_f/\sqrt{2}$ and energy $\epsilon_{\mathbf{k}_1-\mathbf{k}} = \hbar\omega/4$ at −90° (or 90°) relative to $\mathbf{k}_1$. This process is described by the second term on the right-hand side of equation (9). However, the third term is zero, because both momentum and energy conservation are not satisfied by releasing an energy quantum of $\hbar\omega/2$ into the driving field. On the other hand, one atom with $-\mathbf{k}_1$ can collide with one BEC atom, and one of the scattered atoms has momentum k_f at 45° or −45° relative to $-\mathbf{k}_1$. Thus, seeds of four momentum modes at k_f, with 90° relative angular spacing, are generated. Later, when another modulation of frequency ω is applied, those four modes are amplified with pairs of BEC atoms scattering into them. This corresponds to the first term on the right-hand side of equation (9). Finally, those four momentum modes with 90° angular spacing interfere with the BEC to form the D_4 density wave pattern. Note that the D_4 pattern emerges regardless of the presence of the modulation at $\omega/2$ in the pattern-forming stage, so only modulation at ω is applied there.

On the other hand, for D_6 pattern formation under scheme II, a modulation of frequency ω is first applied to generate pairs of opposite momentum modes $\pm\mathbf{k}$ at k_f and energy $\epsilon_\mathbf{k} = \hbar\omega/2$. Then, when the second frequency component $\omega/2$ is added, an atom with $\mathbf{k}$ collides with a BEC atom, absorbing one energy quantum $\hbar\omega/2$ and scattering into atoms with $\mathbf{k}_2$ and $\mathbf{k} - \mathbf{k}_2$ with the same magnitude k_f and energy $\epsilon_{\mathbf{k}_2} = \epsilon_{\mathbf{k}-\mathbf{k}_2} = \hbar\omega/2$ at ±60° relative to $\mathbf{k}$. This corresponds to the hermitian conjugate of the third term on the right-hand side of equation (9). Also, atoms with momentum $\mathbf{k}_2$ or $\mathbf{k} - \mathbf{k}_2$ can collide with one BEC atom into atoms with $\mathbf{k}$, corresponding to the second term on the right-hand side of equation (9). In the meantime, one atom with $-\mathbf{k}$ can collide with one BEC atom and scatter into $-\mathbf{k}_2$ or $-(\mathbf{k} - \mathbf{k}_2)$ at ±60° relative to $-\mathbf{k}$. Thus, six momentum modes with 60° relative angular spacing are generated and are amplified by the ω frequency component at the same time. Eventually, they interfere with the condensate and form the D_6 density wave pattern.

To form a general n-fold symmetric pattern in momentum space, it is necessary to have three different modulation frequencies: two stimulate population into two momentum rings and the other creates coupling between these two momentum rings. Eventually, N momentums will be distributed uniformly on each ring and form an N-fold symmetric pattern in real space by interfering with the BEC. The D_4 and D_6 patterns are the only special cases we know that require fewer than three modulation frequencies. Moreover, the excitation modes associated with these patterns are expected to be squeezed and entangled due to the underlying pair production scattering processes. For example, counter-propagating momentum modes in the D_2 pattern are in a two-mode squeezed state $|\Psi(\tau)\rangle = \frac{1}{\cosh(g\tau)}\sum_{n=0}^{\infty}\tanh^n(g\tau)|n,n\rangle_{\pm\mathbf{k}}$ (ref. [36]), where τ is interaction modulation time and g is the coupling constant (proportional to modulation amplitude). The populations n in counter-propagating modes are always equal and thus maximally squeezed. Similarly, for D_6 patterns, the three pairs of modes with opposite momentum are also squeezed and with additional coupling between different pairs due to the second modulation frequency. We expect them to be in a state with the general form $|\Psi(\tau)\rangle = \sum_{\alpha,\beta,\gamma,\delta=0}^{\infty}C_{\alpha,\beta,\gamma,\delta}(\tau)|\alpha,\beta,\gamma+\delta-\beta,\alpha+\beta-\gamma,\gamma,\delta\rangle_{\mathbf{k}_1,\mathbf{k}_2,\mathbf{k}_3,-\mathbf{k}_1,-\mathbf{k}_2,-\mathbf{k}_3}$, where $\alpha, \beta, \gamma, \delta = 0, 1, 2...$ with constraints $\gamma + \delta \geq \beta$ and $\alpha + \beta \geq \gamma$. $C_{\alpha,\beta,\gamma,\delta}(\tau)$ is a complex amplitude of the Fock state at evolution time $t = \tau$. Due to the conservation of total momentum, the population difference $n_{\mathbf{k}_i} - n_{-\mathbf{k}_i}$ for a pair of opposite momentum modes $\pm\mathbf{k}_i$ is always equal to that of another pair $n_{-\mathbf{k}_j} - n_{\mathbf{k}_j}$. The squeezing and entanglement properties of this state are to be studied in our future experiments.

Principal component analysis. To remove the background of Fourier space in Fig. 2c, we collected 100 images of pure BECs and applied a principal component analysis algorithm to construct the bases and subtract the projection onto these bases from the Fourier transform of BECs with density waves.

We first obtain the Fourier amplitude's magnitude $n_i(\mathbf{k})$ of the ith image of the pure BEC atomic density $n_i(\mathbf{r})$. Each $p \times p$ square matrix $n_i(\mathbf{k})$ is rearranged into a $1 \times p^2$-row vector. All the row vectors are then arranged to form a rectangular matrix M_{ij}, where j ranges from 1 to $p^2 = 121^2$. The mean value of each column is shifted to zero by subtracting the average of experimental realizations, resulting in the data matrix $X = M - \overline{M}$. Our goal is to diagonalize the covariance matrix $X^{\mathrm{T}}X$ to find its eigenvectors w_j and eigenvalues λ_j, which correspond to the statistically independent bases (principal components) and variance of X's projection $X_{ij}w_j$ onto each basis, respectively. We use singular value decomposition to perform this diagonalization.

The first 99 principal components are kept and the corresponding variances are shown in Supplementary Fig. 1a. The average of $n_i(\mathbf{k})$ is counted as an additional basis w_0. In Supplementary Fig. 1b, we plot the average of $n_i(\mathbf{k})$ and the two principal components that have the largest and second-largest variances. Next, we use those constructed bases to remove the background in the Fourier space $n_d(\mathbf{k})$ of the atomic densities of BECs with density waves $n_d(\mathbf{r})$. As an example, in Supplementary Fig. 1c we project one $n_d(\mathbf{k})$ onto all the principal components w_j to reconstruct the background. Finally, the background is subtracted from the original Fourier space and only the signals from density waves are left.

Phases and amplitudes of density waves. To precisely determine the spatial phase of the density waves in different directions, we developed the following fitting procedure. Because the length scale of the density wave we care about is only around k_f, we first filter out the strong low-frequency noise below $0.75k_f$ in the Fourier transform of the in situ density profile $n(x, y)$ and inversely transform it back to obtain the filtered atomic density $\widetilde{n}(x,y)$, as shown in Supplementary Fig. 2a. $\widetilde{n}(x,y)$ is the superposition of plane waves in different directions confined in a finite-sized BEC, so the precision of extracting the phase from its Fourier transform is limited by the small number of density wave periods. To avoid this limitation, we first integrate the filtered atomic density along a certain direction θ normalized by the corresponding integrated circular BEC area to obtain the averaged 1D density oscillation $n_\theta(x) = \int \mathrm{d}y n(x,y)/\sqrt{R^2 - x^2}$. The central part $|x| \leq 10$ μm of $n_\theta(x)$ is then fitted using fit function $f(x) = F_\theta \cos(k_f x + \phi_\theta)$, where F_θ and ϕ_θ are the amplitude and phase of the density wave at k_f and angle θ. The step size of angle θ is chosen to be 1° for better resolution compared to the Fourier transform. The amplitude F_θ and phase ϕ_θ are unaffected by density waves in other directions, which only contribute noise at a spatial frequency smaller than k_f or are completely integrated out.

Supplementary Fig. 2b shows the angular distribution of density wave amplitudes from the Fourier transform compared with that from fitting. It can be seen that the results obtained from these two methods are consistent with each other. For the angles indicated by black arrows in Supplementary Fig. 2b, three examples of the fitting results are shown in Supplementary Fig. 2c. The density oscillation is fit very well when its Fourier amplitude is significant.

Real-space pattern recognition algorithm. We consider each individual in situ absorption image as a combination of several common patterns with random orientations and displacements that contribute to the image with different weights. To reveal the common pattern, we align the strongest components from repeated experimental realizations and the weaker ones are averaged to zero. This alignment can be achieved from our real-space pattern recognition algorithm.

Here, we describe the details of the 2D pattern recognition algorithm (Fig. 3a). We first filter out the low-frequency noise at $|\mathbf{k}| < 0.75k_f$ from the in situ absorption images to obtain a set of $N = 185$ filtered images of atomic density fluctuations, $\widetilde{n}_i(x,y),\ i = 1, \cdots, N$ (Supplementary Fig. 2a). Let $\mathcal{T}_{\theta_i,\mathbf{r}_i}(\widetilde{n}_i)$ denote the result of rotating $\widetilde{n}_i$ by θ_i and then translating by $\mathbf{r}_i$, where we impose the constraint $|\mathbf{r}_i| < 2\pi/k_f$. The objective function L is the spatial variance of the average image $\overline{n}$ after rotating and translating individual images:

$$\overline{n}(\{\theta_i\},\{\mathbf{r}_i\}) = \frac{1}{N}\sum_i \mathcal{T}_{\theta_i,\mathbf{r}_i}(\widetilde{n}_i) \tag{10}$$

$$L(\{\theta_i\},\{\mathbf{r}_i\}) = \frac{1}{S}\int \overline{n}^2 \mathrm{d}x\mathrm{d}y - \left(\frac{1}{S}\int \overline{n}\mathrm{d}x\mathrm{d}y\right)^2 \tag{11}$$

where S is the total area of the atomic density fluctuations. The optimal rotation angles and translation displacements $\{\theta_i\}$ and $\{\mathbf{r}_i\}$ are found by maximizing L, and the pattern recognized is $\overline{n}$ with the optimal parameters.

Because the rotation angle θ_i and displacement $\mathbf{r}_i$ are independent degrees of freedom, we perform optimization of the objective function L in two separate steps. We first find the orientation of each image from the angular distributions of density wave amplitudes F_θ obtained from fitting (Supplementary Fig. 2b). The rotation angles θ_i are changed for individual images in order to maximize the variance of the averaged angular distribution[33]. The angles are then fixed to be the ones after the above optimization, before we optimize the displacement of each image. Finally, we translate each image $\widetilde{n}_i$ by $\mathbf{r}_i$ to maximize the spatial variance of the resulting averaged density fluctuation $\overline{n}$. The recognized common patterns for different modulation schemes are shown in Fig. 3b.

Symmetry decomposition of density patterns. We consider each recognized pattern P shown in Fig. 3b as a superposition of normalized two-, four- and six-fold symmetry components $P_{2,4,6}$ with amplitudes $c_{2,4,6}$ and a small offset c_0. To find the contribution of each symmetry component, we fit the patterns using the following function:

$$P = c_2 P_2 + c_4 P_4 + c_6 P_6 + c_0 \tag{12}$$

where

$$P_2 = \mathcal{R}_{\theta_2}\cos(k_f x + \phi_2) \tag{13}$$

$$P_4 = \frac{1}{\sqrt{2}}\mathcal{R}_{\theta_4}\left[\cos(k_f x + \phi_{4,1}) + \cos(k_f y + \phi_{4,2})\right] \tag{14}$$

$$\begin{aligned} P_6 &= \tfrac{1}{\sqrt{3}}\mathcal{R}_{\theta_6}\Big[\cos(k_f x + \phi_{6,1}) \\ &+ \cos\left(-\tfrac{1}{2}k_f x + \tfrac{\sqrt{3}}{2}k_f y - \tfrac{1}{2}\phi_{6,1} + \tfrac{\sqrt{3}}{2}\phi_{6,2}\right) \\ &+ \cos\left(-\tfrac{1}{2}k_f x - \tfrac{\sqrt{3}}{2}k_f y - \tfrac{1}{2}\phi_{6,1} - \tfrac{\sqrt{3}}{2}\phi_{6,2}\right)\Big] \end{aligned} \tag{15}$$

Here, $\mathcal{R}_\theta[\cdot]$ denotes rotation by angle θ. There are 12 fitting parameters in total: $\{c_2, c_4, c_6\}$ determine the strengths of the symmetry components, c_0 determines the overall offset, $\{\theta_2, \theta_4, \theta_6\}$ determine the orientations and $\{\phi_2, \phi_{4,1}, \phi_{4,2}, \phi_{6,1}, \phi_{6,2}\}$ determine the displacements. The optimal fitting parameters are provided in Supplementary Table 1. One example of the symmetry decomposition results for the D_6 density pattern under scheme II is shown in Supplementary Fig. 3.

Data availability

The data represented in Figs. 2d, 3c, 4b,f are available as Source Data Figs. 2, 3 and 4. All other data that support the plots within this paper are available from the corresponding author upon reasonable request.

References

34. Abe, H. et al. Faraday instability of superfluid surface. *Phys. Rev. E* **76**, 046305 (2007).
35. Hung, C.-L. et al. Extracting density–density correlations from in situ images of atomic quantum gases. *New J. Phys.* **13**, 075019 (2011).
36. Hu, J., Feng, L., Zhang, Z. & Chin, C. Quantum simulation of Unruh radiation. *Nat. Phys.* **15**, 785–789 (2019).
37. Petrov, D. S., Holzmann, M. & Shlyapnikov, G. V. Bose–Einstein condensation in quasi-2D trapped gases. *Phys. Rev. Lett.* **84**, 2551–2555 (2000).

Acknowledgements

We thank K. Patel for careful reading of the manuscript. This work is supported by National Science Foundation (NSF) grant no. PHY-1511696, the Army Research Office Multidisciplinary Research Initiative under grant no. W911NF-14-1-0003 and the University of Chicago Materials Research Science and Engineering Center, which is funded by the NSF under grant no. DMR-1420709. J.H. acknowledges financial support from the National Natural Science Foundation of China under grant no. 11974202.

Author contributions

Z.Z. and K.-X.Y. performed the experiments, built the theoretical model and analysed the data. L.F. contributed to development of the modulation hardware and pattern recognition scheme. J.H. contributed to the discussion of the results. C.C. supervised the work. All authors contributed to writing the manuscript.

Competing interests

The authors declare no competing interests.

Additional information

Supplementary information is available for this paper at https://doi.org/10.1038/s41567-020-0839-3.

Correspondence and requests for materials should be addressed to C.C.

Peer review information *Nature Physics* thanks Simon Cornish and other, anonymous, reviewer(s) for their contribution to the peer review of this work.

Reprints and permissions information is available at www.nature.com/reprints.